



**HAL**  
open science

# On the use of bi-species ZDES for multi-nozzle space launcher configurations

Jolan Reynaud, Pierre-Elie Weiss, Sébastien Deck

► **To cite this version:**

Jolan Reynaud, Pierre-Elie Weiss, Sébastien Deck. On the use of bi-species ZDES for multi-nozzle space launcher configurations. *Flow, Turbulence and Combustion*, In press, 10.1007/s10494-022-00372-4 . hal-03813449

**HAL Id: hal-03813449**

**<https://hal.science/hal-03813449>**

Submitted on 13 Oct 2022

**HAL** is a multi-disciplinary open access archive for the deposit and dissemination of scientific research documents, whether they are published or not. The documents may come from teaching and research institutions in France or abroad, or from public or private research centers.

L'archive ouverte pluridisciplinaire **HAL**, est destinée au dépôt et à la diffusion de documents scientifiques de niveau recherche, publiés ou non, émanant des établissements d'enseignement et de recherche français ou étrangers, des laboratoires publics ou privés.

# On the use of bi-species ZDES for multi-nozzle space launcher configurations

Jolan Reynaud<sup>1</sup>, Pierre-Elie Weiss<sup>1\*</sup> and Sbastien Deck<sup>1</sup>

<sup>1\*</sup>DAAA, ONERA, The French Aerospace Lab, Meudon, 92190, France.

\*Corresponding author(s). E-mail(s): [pierre-elie.weiss@onera.fr](mailto:pierre-elie.weiss@onera.fr);  
 Contributing authors: [jolan.reynaud@onera.fr](mailto:jolan.reynaud@onera.fr);  
[sebastien.deck@onera.fr](mailto:sebastien.deck@onera.fr);

## Abstract

Space launchers experience high fluctuating pressure levels during the ascent (for both expendable and reusable launch vehicles) and return phases (for reusable launch vehicles only). To simulate the fluctuating pressure field occurring on such configurations accurately, a numerical workflow combining ZDES Mode 2 (2020) and a hybrid scheme ensuring robustness in shock wave regions and low dissipation levels in vortical regions is used in the framework of bi-species inert flows. The assessment of the performance of this numerical strategy is based on the simulation of a four-nozzle launcher model previously studied experimentally by Musial and Ward [1]. A comparison of pressure coefficients shows that ZDES gives an improvement in the capability of predicting the base pressure over standard RANS models. Spectral analysis of the fluctuating pressure at the wall shows that the flow is dominated by the antisymmetric mode  $m = 1$  contributing to up to 80% of the energy at a dimensionless frequency  $St_D = 0.2$ .

**Keywords:** multi-nozzle afterbodies, supersonic jets, turbulence modelling, bi-species flow, RANS/LES, ZDES

## 1 Introduction

CFD is playing an expanding role in the aerospace industry and enhancing its capabilities to simulate complex unsteady turbulent flows is considered as a major objective in the field [2, 3]. As an example, to support the development of multi-nozzles for reusable launcher designs, the accurate prediction of afterbody flows occurring

behind the base and around the nozzles during flight is of primary importance to assess the aerodynamic performance and the integrity of the vehicles. Indeed, the reactive multi-gas interactions occurring between the hot propulsive jets and the base flow can induce adverse phenomena such as base drag, due to the low pressure recirculation zone forming behind the base. The pressure loads in this area can damage mechanical structures. Moreover, base heating attributable to the recirculation of hot gases towards the base may arise. As a result of this complexity, the aerodynamic design of new generation launcher afterbodies remains a challenge for both experimental and numerical tools.

As far as numerical approaches are concerned, two main challenges are classically acknowledged in the literature. First, the need to resolve the large-scale turbulent eddies driving the dynamics of base flows in order to get accurate predictions of the wake flow topology and wall pressure levels has been well documented for generic space launcher configurations (Reynaud et al. 2021 [4] and Statnikov et al. 2016 [5]). RANS approaches have indeed shown limited capacities to reproduce such massively separated flows whereas RANS/LES approaches, combined with low dissipative numerical schemes, have displayed a good cost/accuracy compromise (Pain et al. 2014 [6], Weiss and Deck [7]). Then, authors such as Gusman et al. 2011 [8] have advocated the need to take into account the thermodynamic properties of the hot reactive propulsive jets to increase the representativeness of space launcher simulations. As the computational cost of both RANS/LES approaches and multi-species reactive flow models is important, authors often have to establish a compromise between an accurate treatment of turbulence and the representation of chemistry effects.

Regarding wind tunnel experiments, only few studies have been dedicated to multi-nozzles space launcher configurations with hot propulsive jets (Mehta et al. 2013 [9]). Among them, the case of a four-JP4/LOX-nozzle space launcher configuration studied experimentally in Musial and Ward 1961 [1] is considered as a reference case and has been studied numerically by several authors. Among these studies, Mehta et al. 2013 [9] and Pu and Jiang 2019 [10] employed advanced thermodynamic models but only used RANS models for turbulence modelling. Though these studies have provided useful analyses of the flow field, noticeable errors in the evaluation of wall pressure levels have been reported as well.

To contribute to the study of launcher base flow prediction methods, this article presents a numerical study of a four-nozzle space launcher configuration using a scale resolving framework based on the use of a simple two-species physical model and hybrid numerical methods in order to be able to do scale-resolving simulations at an affordable cost. The hybrid model used is the ZDES mode 2 (2020) model by Deck and Renard 2020 [11]). The results will be compared with a two-species RANS computation and with RANS computations including chemistry effects from the literature in order to investigate the benefits of a scale resolving approach for multi-nozzle afterbody computations.

In the following, the test case as well as the salient features of the numerical framework used for the bi-species ZDES and RANS computations are first briefly described before going into the instantaneous and Reynolds averaged properties of the flow. In particular, the focus is put on the resulting wall pressure distribution

on the base and on the nozzles of the launcher. Finally, the salient features of the fluctuating pressure field are investigated with second-order statistics and spectral analyses.

## 2 Test case and mesh setup

The present study is based on a wind tunnel experiment provided by Musial and Ward [1], the geometry of the model for this study is shown in Fig.1. It consists of a four-nozzle subscale rocket model defined by the following parameters  $r_b = 152.4$  mm,  $L_n/D_e = 1.53$ , and  $D_s/D_e = 1.67$ . The four rocket engines operate with a propulsive mixture combining JP-4 as a fuel and LOX as an oxidizer. The selected flow conditions for pressure correspond to a flight altitude of 14.9 km and are summarized in Table 1 together with the total pressure  $P_c$  and total temperature  $T_c$  inside the combustion chamber. These test conditions correspond to underexpanded jets with an exit Jet Pressure Ratio (JPR=3.4) (Mehta et al. 2013 [9]). The wind tunnel model was instrumented with pressure transducers and temperature probes on its base.

As shown in Fig.2b a structured mesh has been designed using a secondary O-H topology for each of the nozzles and a main O-H topology built around the launcher body. The radial point distribution shown in Fig.2a is set such that  $\Delta y^+ \approx 1$  is ensured for every attached boundary layer with exponential expansion ratios lower than 1.05 and to cluster points in the mixing layer forming behind the main body base. The computational domain extends over 5 times the length  $L_c$  of the main body ( $1L_c$  upstream and  $3L_c$  downstream) and has a global radius that is equal to 5 times the radius of the base. The domain ends with a sponge region and non-reflective boundary conditions to avoid any spurious numerical waves. With 240 points in the azimuthal direction ( $\Delta\theta = 1.5^\circ$ ) the mesh contains  $55.6 \times 10^6$  cells overall.

Parameters	Values
$P_c$	41.37 bar
$T_c$	3469.8 K
$P_\infty$	12209.5 Pa
$T_\infty$	297.7 K
$M_\infty$	2.75

**Table 1:** Low altitude case initial flow conditions (Musial & Ward 1961 [1]).  $\cdot_c$  refers to the nozzle chamber conditions.

## 3 Computational set-up

### 3.1 Two-species model

To study the 4-nozzle launcher configuration, an implicit finite volume formulation of the two-species Navier-Stokes equations, presented in Reynaud et al. 2022 [12] is

## 4 On the use of bi-species ZDES for multi-nozzle space launcher configurations

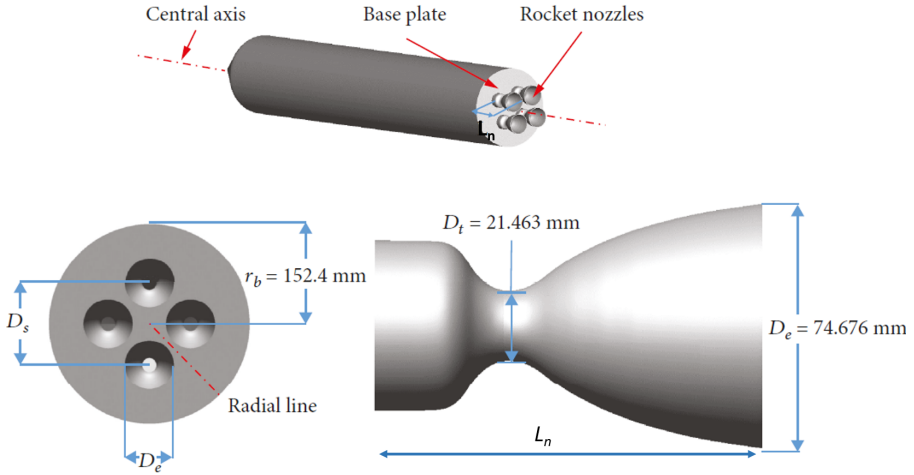
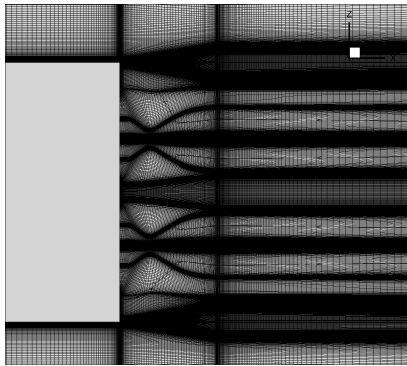
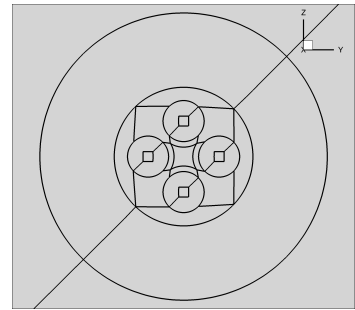


**Fig. 1:** Schematic view of the 4-nozzle launcher geometry (from Pu and Jiang 2019 [10])



(a) Mesh distribution in the nozzles exit area



(b) 4 secondary O-H topologies included in a main O-H topology describing the engine bay

**Fig. 2:** Mesh description

used. This approach enables to define the propulsive gas mixture and the surrounding air as two perfect gases. In the following, all relevant quantities for the jet gas are indicated by the subscript  $j$ . To provide adequate properties for the propulsive mixture, JP-4/LOX equilibrium flow data from Huff et al. 1956 [13] are used to define constant values for the Sutherland's law constants  $[\mu_{0j}, S_j, T_{0j}]$ , the specific heat ratio  $\gamma_j$ , the volume constant heat ratio  $c_{vj}$ , the Prandtl number  $Pr_j$  of the jet gas and a turbulent Prandtl number  $Pr_t$  (see Tab.2). The turbulent Schmidt number is chosen as 0.5 for the mixing between air and the propulsive mixture. Many authors (*e.g.* Baurle & Edwards 2010 [14], Clifton & Cutler 2007 [15]) have shown the dramatic importance of the value of the turbulent Schmidt number  $Sc_t$  on RANS results.

However, Reynaud et al. 2021 [16] have shown that conversely to RANS methods, a weak dependence to  $S_{c_t}$  values is observed for scale resolving simulations. Thanks to the reduced influence of unresolved turbulent fluctuations, these authors have shown that their numerical predictions with the scale resolving ZDES computations appear almost independent of  $S_{c_t}$ . This weak dependence of the numerical assessments with regards to  $S_{c_t}$  (similarly with  $Pr_t$ ) is precisely one of the interest to resorting to scale resolving simulations since the large-scale mixing processes are mostly resolved rather than modelled.

$\mu_{0_j}$ (N.s/m <sup>2</sup> )	$1.85 \cdot 10^{-5}$
$T_{0_j}$ (K)	370
$S_j$ (K)	168
$\gamma_j$	1.224
$cv_j$ (J.kg <sup>-1</sup> .K <sup>-1</sup> )	1997.5
$Pr_j$	0.78
$Pr_t$	0.90

**Table 2:** Properties of the perfect gas simulating a JP4/LOX mixture

## 3.2 Numerical set-up

### 3.2.1 Numerical method

The FLU3M code developed by ONERA solves the compressible Navier-Stokes equations on multiblock structured grids. The accuracy of the solver for DNS, LES and hybrid RANS/LES purposes has been assessed in various applications including transitional flows (Mary & Sagaut 2002 [17]), wall-bounded turbulent flows (Pamies et al. 2009 [18]; Gand et al. 2010 [19]; Deck et al. 2014 [20], Deck et al. 2018 [21]), massively separated flows (Simon et al. 2007 [22]; Larcheveque et al. 2004 [23]; Weiss et al. 2009 [24]; Weiss & Deck 2013 [25], Weiss & Deck 2018 [7]). In these last references, the numerical results are thoroughly compared with the available experimental data of both Reynolds averaged quantities as well as pressure and velocity fluctuations including spectral and second-order analysis.

The time integration is carried out by means of the second-order-accurate backward scheme of Gear. Newton-like inner iterations (typically 4) are used to reach second-order time accuracy. A decrease of the inner-residuals of at least one order is obtained. Besides, the time step needs to be chosen in order to correctly describe the important physical phenomena (such as mixing layer and wake dynamics) which are being simulated. The Courant-Friedrichs-Levy (CFL) condition relates the maximal allowable time step to a local velocity and local mesh spacing. The acoustic  $CFL_a$  number based on maximum acoustic velocity  $U + a$  (where  $U$  and  $a$  denote respectively the local velocity magnitude and speed of sound) and the grid step taken as

the minimum grid extension spacing in each direction, namely:

$$CFL_a = \frac{(U + a)\Delta t_{CFD}}{\min(\Delta x, \Delta y, \Delta z)} \quad (1)$$

In the present study, the time-step for the ZDES computations is set to  $\Delta t_{CFD} = 2.10^{-7} s$  yielding  $CFL_a \leq 6$  in the base flow mixing layer. The highest values are observed in the very early stages of the mixing layer due to the fine grid cells inherited from the attached boundary layer in the frame of a structured mesh. One can note that the corresponding CFL value based only on the maximum hydrodynamic velocity  $U$  is lower than one (*i.e.*  $CFL = \frac{U\Delta t_{CFD}}{\min(\Delta x, \Delta y, \Delta z)} \leq 1$ ) in the whole massively separated flow region of interest.

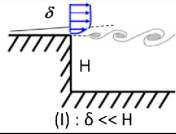
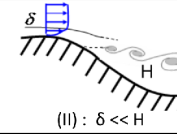
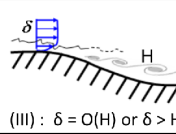
The choice of the spatial scheme deserves particular attention when scale resolving simulations in a supersonic framework are considered since the scheme has to challenge conflicting demands between accuracy in LES regions (*i.e.* low numerical dissipation) and robustness for shocks. Hence, Reynaud et al. [4] developed a hybrid numerical framework based on Ducros's sensor [26] and designed to switch from a low-dissipation formulation in presence of vortical structures to a robust formulation around high gradients. In practice, the scheme relies on a salient combination of the AUSM+ (Liou 1996 [27]) for shocks and an adapted low-dissipative AUSM+(P-LD) (Mary & Sagaut 2002 [17]) in the resolved turbulence region. The numerical dissipation of the spatial scheme is dynamically optimized based on local properties, especially for turbulent flows containing shocks.

Further details concerning the numerical method and implementation of turbulence models can be found in Pechier, Guillen & Cayzac (2001) [28], Deck et al. (2002)[29] while the numerical framework dedicated to the resolution of bi-species flows is thoroughly detailed in the paper by Reynaud et al. [12].

### 3.2.2 Turbulence modelling

The ZDES approach developed by ONERA [30, 31] belongs to the family of multi-resolution approaches which covers the full range of modeling from RANS to Wall-Modelled LES (WMLES) [21, 32, 33] and aims at treating in a simple model all classes of flow problems indicated in Fig. 3. The zonal nature of ZDES permits the use of various model formulations within the same computation (see Deck & Laraufe [34] for an example).

The current study is solely based on ZDES mode 2 (2020) [11], a fully automatic model where the model sets dynamically by itself the RANS and LES branches (*i.e.* the RANS and LES zones are not set in advance by the user). In the frame of the underlying Spalart-Allmaras model [35],  $\tilde{d}_{ZDES}^{mode 2}$  replaces the distance to the wall  $d_w$

Zonal Detached Eddy Simulation (ZDES)			
	Mode 1	Mode 2	Mode 3
Flow category	 (I) : $\delta \ll H$	 (II) : $\delta \ll H$	 (III) : $\delta = O(H)$ or $\delta > H$
Applications	Base flow, free shear flows, spoilers, steps, slat/flap cove, etc.	Buffet, flaps, duct flows, nacelle intake, etc.	Corner flows, turbulent boundary layer, separation onset on high lift devices, shallow separations, etc.

**Fig. 3:** Classification of typical flow problems, associated ZDES modes and examples of applications. *mode 1*: separation fixed by the geometry, *mode 2*: separation induced by a pressure gradient on a curved surface, *mode 3*: separation strongly influenced by the dynamics of the incoming boundary layer. RANS (*mode 0*) is the default mode (adapted from Deck[31]).

involved in the SA model according to:

$$\tilde{d}_{ZDES}^{mode 2} = f \left( \tilde{\Delta}, d_w, U_{i,j}, \nu, \tilde{\nu}, \frac{\partial \tilde{\nu}}{\partial n}, \frac{\partial \omega}{\partial n} \right) \quad (2)$$

with  $\tilde{\Delta}(\Delta x, \Delta y, \Delta z, \vec{\omega})$  denoting the subgrid length scale entering  $\tilde{d}_{ZDES}^{mode 2}$  that depends on the grid cell size,  $U_{i,j}$  the velocity gradients,  $d_w$  the distance to the wall,  $\omega$  the magnitude of vorticity,  $\nu$  and  $\tilde{\nu}$  the kinematic and pseudo eddy viscosity as well as  $\partial/\partial n$  the derivative in the wall-normal direction. The definition of  $\tilde{d}_{ZDES}^{mode 2}$  is not a minor adjustment in the DES framework since the modified lengthscales depend not only on the grid but also on the velocity and eddy viscosity fields and their wall-normal derivatives. ZDES mode 2(2020) is to the authors' best knowledge the only published formulation providing a safe RANS shielding of the whole turbulent boundary layer profile for any grid cell size (including infinite mesh refinement) and pressure gradient even when the separation moves in time (see [11] for an example of transonic buffet over a supercritical airfoil).

Figure 4 displays an instantaneous snapshot of the eddy viscosity in a plane of symmetry of the current configuration. The attached turbulent boundary layer treated in RANS mode is clearly identified. The eddy viscosity in the base region (*i.e.* LES region) is not destructed as fast as in ZDES mode 1 calculation (see [36] for example), but the impact in the resolved turbulence seen in Figure 6a is marginal. Let us be reminded that within ZDES mode 2 (2020) the RANS and LES domains are not set in advance by the user (unlike as in mode 1) so that mode 2 appears as a good compromise between efficient shielding of attached boundary layers and destruction of eddy viscosity in the free shear layer.



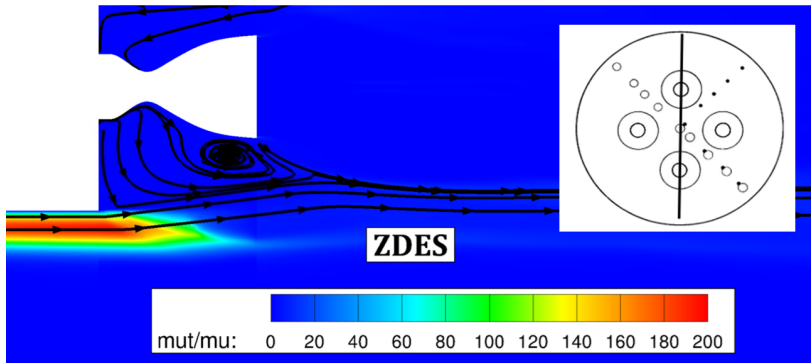


**Fig. 4:** Instantaneous eddy viscosity field.

## 4 Results

### 4.1 Flow topology

#### 4.1.1 Instantaneous flow topology

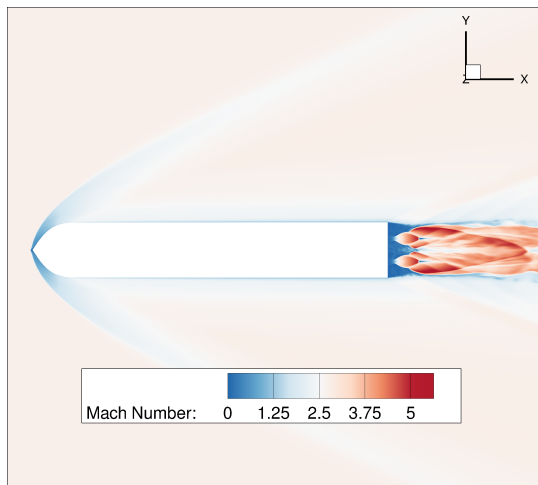
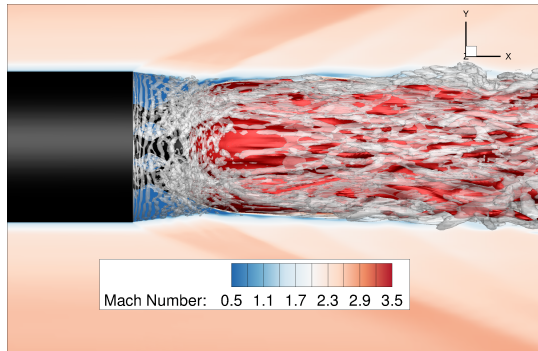
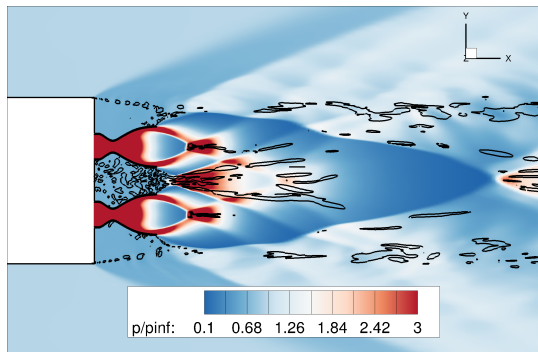


**Fig. 5:** Instantaneous Mach number distribution

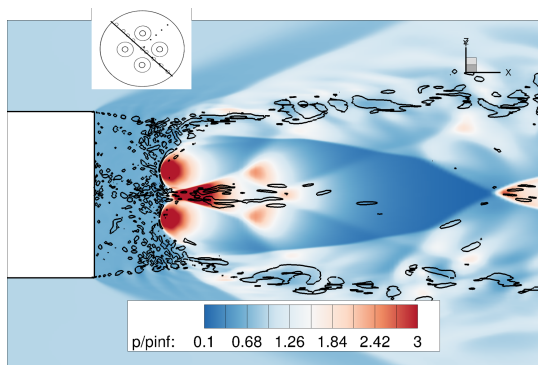
A general view of the flow around the launcher is displayed in figure 5. The instantaneous visualisation of the Q-criterion in the wake flow is then shown in Fig.6a. It enables to observe that the main body boundary layer separates at the base and that coherent structures roll up into azimuthal vortices to form a mixing layer which bends towards the launcher axis under the effect of an expansion wave. As displayed in the instantaneous pressure field shown in Fig.6b, a realignment shock forms as the bended flow meets with the propulsive jets boundaries and induces an adverse



(a) Mach number distribution and iso-surface of Q-criterion in the wake of the afterbody



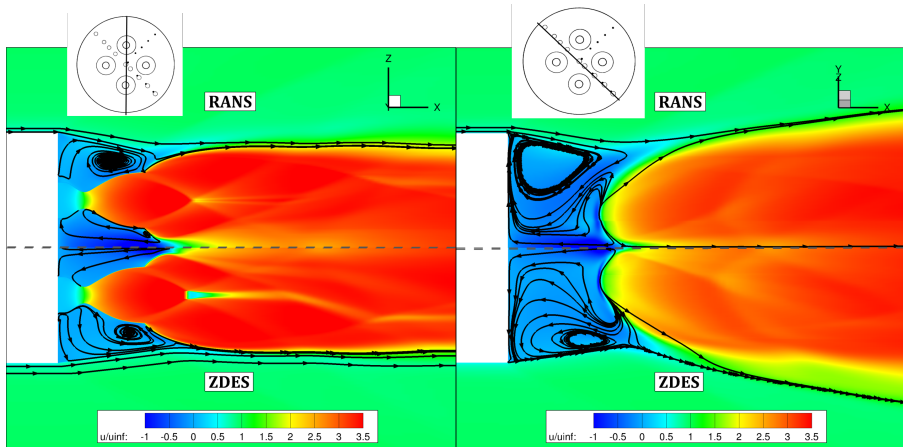
(b) Instantaneous pressure distribution and Q-criterion (black iso-lines) in the wake of the launcher in a plane containing two nozzles.



(c) Instantaneous pressure distribution and Q-criterion (black iso-lines) in the wake of the launcher in a plane between the nozzles

**Fig. 6:** Instantaneous flow topology

pressure gradient on the outer side of the jet boundaries. Looking at the underexpanded propulsive jets, we observe that in accordance with results from Mehta et al. 2013 [9] and Pu and Jiang 2019 [10], the jet boundaries collide near the axis of the



(a) Distribution of longitudinal velocity and streamtraces in a plane containing two nozzles. (b) Distribution of longitudinal velocity and streamtraces in a plane between the nozzles

**Fig. 7:** Average dimensionless velocity distribution in the wake of the launcher

launcher and create a high pressure zone on the inner side of the jet boundaries. These high pressure gradient zones together with the normal shocks visible inside the jets justify the use of hybrid numerical methods able to capture shocks while maintaining a low numerical dissipation in the rest of the flow to resolve turbulent structures. One can indeed note in Fig. 6b that in addition to the azimuthal vortices issuing from the base, the mixing process between the jets yield the formation of a wide variety of turbulent structures in the inter-nozzle area. To complete the description of the organisation of the flow in this area, a cutting plane located between the nozzles is presented in Fig. 6c. On both sides of the main high-pressure zone corresponding to the confluence of the four jets, two secondary high-pressure zones can be observed. Analysing the turbulent structures forming in the afterbody area, one can note that interactions occur between the structures from the main annular mixing layer and the structures from the interaction of the jets.

#### 4.1.2 Mean flow topology

The Reynolds averaged field is computed on the fly during the unsteady ZDES calculation. As the vortex shedding period related to the base diameter was estimated to be  $T_s = \frac{2*r_b}{0.2*U_\infty} \approx 1.6$  ms, a period of 32 ms =  $20 \times T_s$  was adopted to clear the flow from transient effect before using a 80 ms  $\approx 50 \times T_s$  period to compute statistics. As an example, figures 7a and 7b display the mean velocity field as well as pseudo streamlines for both RANS and ZDES calculations. First, looking at a longitudinal plane containing two nozzles (Fig. 7a), one can observe the formation of a recirculation zone on the outer side of the nozzles. This recirculation zone interacts with the propulsive jets which entrain the external flow through a mixing layer. This entrainment effect appears stronger in the RANS computation as the recirculation bubble reattaches closer to the nozzle exit in the RANS computation ( $\frac{X_r}{L_n} = 1.10$ ) than in the

ZDES computation ( $\frac{X_r}{L_n} = 1.35$ ). This first flow pattern corresponds to the one usually observed for axisymmetric base flow with a single nozzle (Reynaud et al. 2021 [4], Statnikov et al. 2016 [5]). Due to the expansion of the jets, one can notice that the area delimited by the launcher base, the nozzle wall and the jet boundary displays similarities with a supersonic cavity geometry with a  $L_c = X_r$  length (corresponding the location of the reattachment) and a  $L_c/De_c \approx 2$  depth ratio with  $De_c$  its depth. Such an analogy, used experimentally by Wong et al. [37], is described in Fig.8 presenting parameters  $L_c$  and  $De_c$ . In the present case, the cavity analogy concerns the geometrical area formed by the base and a nozzle.

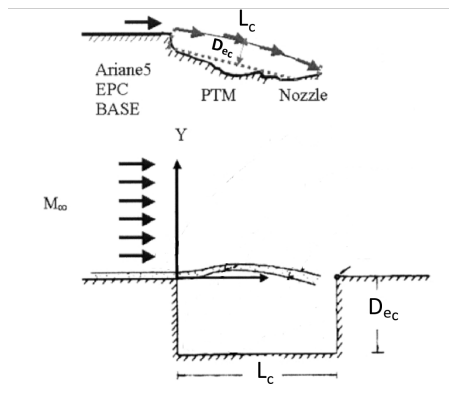


**Fig. 8:** Analogy between the afterbody area and a supersonic cavity, adapted from Wong et al. [37].

In the present case with four propulsive nozzles, additional flow interactions occur. Indeed, due to the impingement between the supersonic propulsive jets, the fluid located between the nozzles (see Fig.7b) is subject to a strong adverse pressure gradient that leads to a reverse flow heading towards the base. We note that the RANS computation provides a higher reverse velocity than what is observed in the results from the ZDES simulation similarly to what is observed for single axisymmetric base flows (see Simon et al. [38]). This reverse flow impacts the base and induces the formation of radial wall jets. In a plane containing nozzles (see Fig.7a), these wall jets will be deflected as they go around a nozzle and part of the reverse flow will regain a positive longitudinal velocity. In a plane located between the nozzles (see Fig.7b), these wall jets are pushed towards the base outer radius and feed the external recirculation zone. In such a plane, the prediction of the recirculation zone topology again differs between the two computations as the S-A model predicts a center position of the recirculation closer to the base than ZDES. Despite some local differences, the two bi-species computations are able to reproduce the main flow features of a 4-nozzle launcher wake flow (Mehta et al. 2013 [9]).

### 4.1.3 Gas mixing

To investigate the interaction between the propulsive jets and the base flow further, the average distribution of the propulsive mixture mass fraction ( $Y_{fuel}$ ) in the afterbody area is displayed in Fig. 9. One can note that the RANS computation predicts a much more intense mixing between the two gases than the ZDES computation. This is shown by the greater predicted growth rate of the jet external mixing layer and by  $Y_{fuel}$  levels in the inter-nozzle area nearly twice as high as those found with ZDES. Such discrepancies in the amount of hot propulsive gases advected back to the base area can be attributed to the strong influence of the turbulent Schmidt number on RANS mixing prediction (Reynaud et al. 2021 [16]) and is expected to lead to differences in base temperature predictions. This influence is strongly minimized thanks to the use of ZDES where turbulence in the base region is mostly resolved.

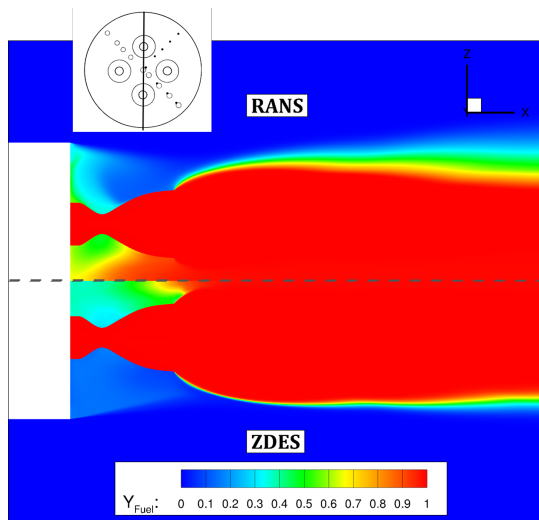


**Fig. 9:** Distribution of the fuel mass fraction in a plane containing the nozzles.

## 4.2 Base pressure distribution

In order to guide the design of future space launchers, numerical methods have to predict the base drag and the mechanical loads resulting from the previously described flow topology accurately.

As an example, Mehta et al. 2013 [9] performed computations with different levels of physical modelling for the propulsive jets; a frozen flow computation (Me1) where the propulsive mixture is considered as a perfect gas with a fixed  $\gamma_j=1.15$  (value corresponding to chamber conditions); a variable  $\gamma_j$  computation (Me2) where  $\gamma_j$  is a function of temperature and a reactive computation (Me3) where the propulsive gas is modelled as a 10-species mixture and chemical reactions are taken into account. Then, in Pu and Jiang 2019 [10] several RANS models were tested to perform reactive computations.

Looking at the base pressure coefficient distributions displayed in Fig. 11, results from Metha et al. 2013 [9] showed that, with the Menter BSL (Baseline) RANS model, the use of the simplest physical model (referred to as Me1) surprisingly provided the best predictions for base pressure levels as both the variable  $\gamma_j$  computation (referred to as Me2) and the reactive computation (referred to as Me3) lead to a significant underestimation of base pressure levels in comparison with experimental data. The same magnitude of error is found in Pu and Jiang 2019 [10] as shown here with the predictions obtained with the RNG (Renormalization Group) turbulence model (Pu RNG), which provided the best results in their study. One can furthermore observe that all of the mentioned RANS computations are unable to reproduce the almost flat pressure profile found experimentally as they induce an overestimation of the pressure difference occurring between the center of the base and the outer radius. These discrepancies motivate the use of more advanced turbulence modelling such as the ZDES approach used here. Focusing on base pressure coefficient distributions obtained with the present computations, one can note that the use of an equilibrium flow hypothesis in the nozzles (with  $\gamma_j=1.224$ ) provides predictions coherent with numerical results from the literature, in between the frozen flow computation and the computations including chemistry effects. The use of ZDES improves predictions in comparison with RANS as it recovers a flat pressure profile and higher pressure levels near the outer radius. These disparities can be linked to the previously observed differences in the topology of the recirculation zone (i.e. characteristic sizes and maximum backflow velocity).

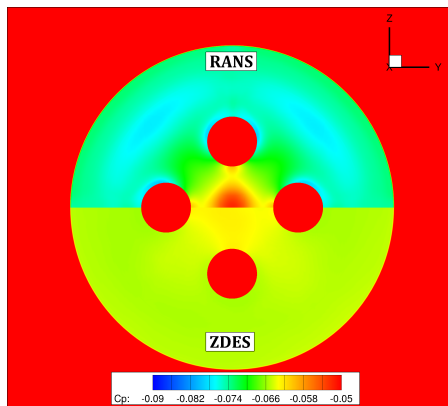


**Fig. 10:** Pressure coefficient iso-contours at the afterbody base (Top: RANS, Bottom: ZDES).

### 4.3 Nozzle pressure distribution

As reminded in the introduction, the accurate prediction of the engine bay environment and especially on the base is of major importance. As an example, the mean wall pressure ( $C_p = \frac{P - P_\infty}{\frac{1}{2} \gamma_{air} P_\infty M_\infty^2}$ ) distributions predicted on the base and on the

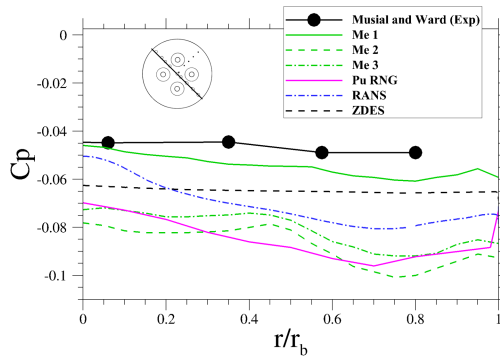


**Fig. 11:** Base pressure distribution along an inter-nozzle radial line

external walls of the nozzles are displayed in Fig.12a (RANS) and Fig.12b (ZDES). For each simulation, similar pressure fields are predicted on the four nozzles. Notable differences are however observed when comparing the two computations for both the pressure levels and the spatial variation of  $C_p$ .

To analyse these differences, the evolution of the pressure coefficient ( $C_p$ ) has been studied along generating lines located at different angular locations (outer position (OUT), inner position (IN) and side positions (SIDE)) on a nozzle external wall as displayed in Fig.13. The obtained pressure profiles are displayed in Fig.14 and reveal the deviations between the RANS and the ZDES computations. Indeed, the use of ZDES provides relatively flat  $C_p$  profiles (close to  $C_p = -0.065$ ) on every position around the nozzle whereas the RANS calculation predicts noticeable pressure axial variations for each location around the nozzle and a substantial pressure gap between the inner position and the outer position. Each turbulence modelling approach would thus lead to different estimations of the fluctuating pressure field used to study the mechanical behaviour of the nozzles. Based on previous numerical results obtained on launcher configurations with a single nozzle (Pain et al. 2014 [6], Reynaud et al. 2021 [4]) one can note that the ZDES predictions are used to be more representative than the RANS ones.

#### 4.4 Pressure fluctuations in the engine bay

To get a better understanding of the unsteady properties of the base pressure field, the unsteady pressure data obtained from the ZDES computation are investigated in the engine bay. First, as a consequence of the unsteady interactions occurring between the different flow features described in the previous section, the instantaneous distribution of wall pressure coefficient ( $C_p$ ) shown in Fig.15a, displays no symmetry and can be used to estimate the risk of nozzle vibrations due to side-loads. The rms value of pressure fluctuations namely the  $C_{p_{rms}}$  ( $C_{p_{rms}} = \frac{p_{rms}}{q_\infty}$  with  $q_\infty = \frac{1}{2}\gamma p_\infty M_\infty^2$  the dynamic pressure) distribution on the launcher walls is displayed in Fig. 15b.

The pressure fluctuations levels observed on the base lie in the range [0.001, 0.0025], such values are lower than the ones reported in [39] ( $C_{p_{rms}} \approx 0.004$ ) for a blunt base flow with a similar Mach number. The presence of the nozzles

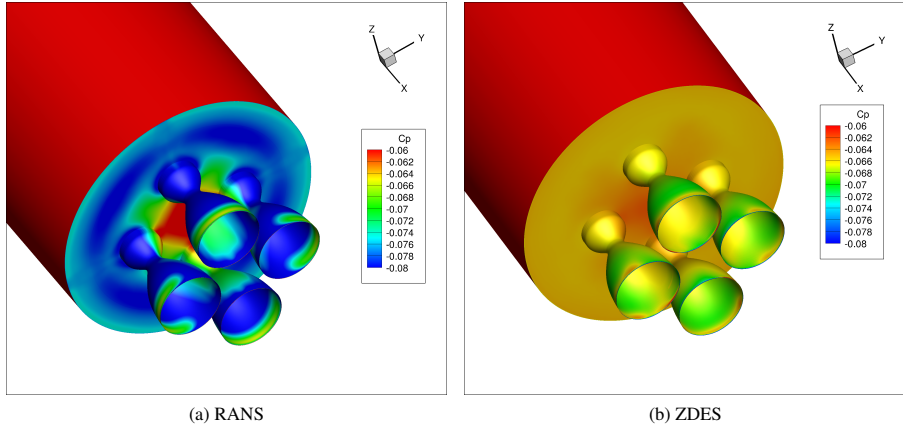


**Fig. 12:** Distribution of mean wall pressure coefficient predicted on the external walls of the launcher.

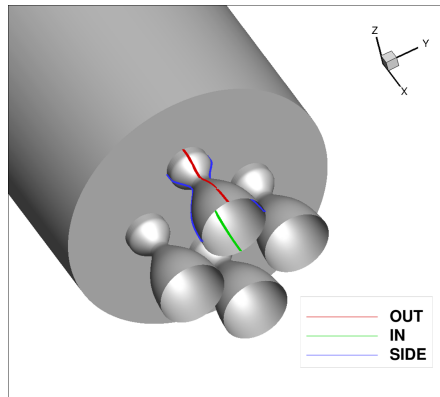


**Fig. 13:** Angular positions of the generating lines along the nozzles.

and the jets thus seem to have a stabilizing effect on the level of pressure fluctuations occurring at the base.

Looking at the propulsive nozzles, the maximum fluctuation levels ( $Cp_{rms} > 0.01$ ) are located on the edge of every nozzles near the launcher axis. To analyse the pressure fluctuations further, the next sections describe their evolution in selected areas: a ring located on the base  $r/r_b = 0.85$  shown in Fig.16 as well as the lines along the nozzle walls presented in Fig13.

The azimuthal distribution of  $Cp_{rms}$  on the ring  $r/r_b = 0.85$  (Figure 17) displays a quasi-periodic variation of the pressure fluctuation intensity with peaks located between the nozzles ( $45^\circ, 135^\circ, 225^\circ, 315^\circ$ ) and an important decrease around locations aligned with the center of the nozzles ( $0^\circ, 90^\circ, 180^\circ, 270^\circ$ ). The amplitude of  $Cp_{rms}$  is not exactly the same and can partly be attributed to the limited



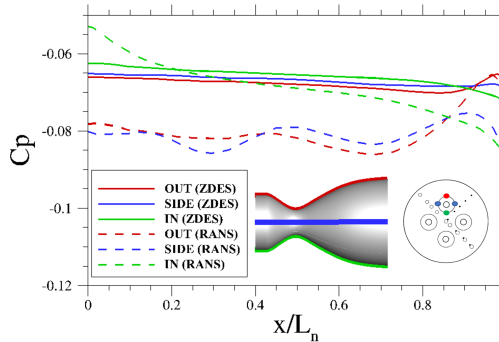


**Fig. 14:** Axial evolution of  $C_p$  at different angular locations along a nozzle

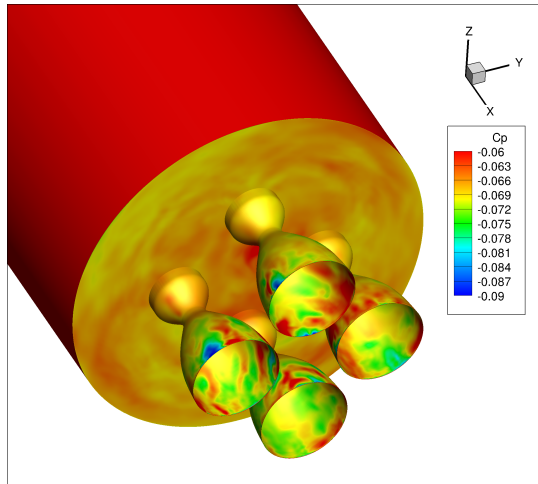
duration of the calculation. Nevertheless one can note that discrepancies between the extrema (*e.g.* between peak 1 and peak 2) correspond to small levels typically  $P_{rms} \approx 0.023\%$  of the dynamic pressure.

These observations confirm the stabilizing effect of the nozzle wall and jet as reported by Deck and Thorigny [40].

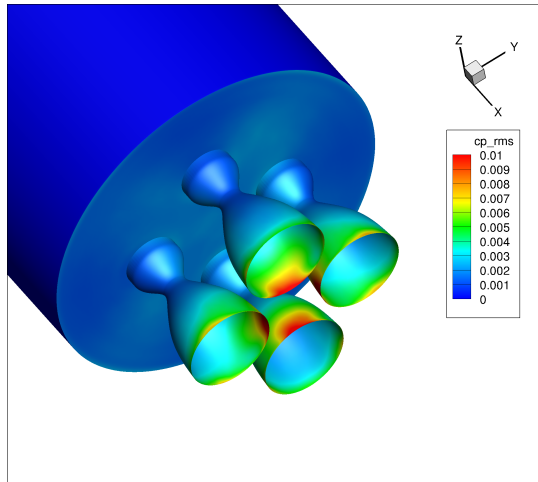
The evolution of the fluctuating pressure coefficient along the nozzles is then presented in Fig. 18. The overall increase of fluctuating pressure levels in the direction of the flow observed with the present computation is in line with previous RANS/LES results and measurements described in Statnikov et al. 2016 [5] on a launcher with one nozzle placed in an external flow at  $M_\infty = 3$ . Furthermore, the computed fluctuation levels are in the same range as the ones reported by Statnikov et al. 2016 [5] with  $Cp_{rms} \in [0.0015, 0.01]$ . Important differences are however observed depending on the angular position. Indeed, the inner side of the nozzle is subject to pressure fluctuations twice as high as the outer side.

To complete this description, one can note that the predicted fluctuation levels for this supersonic configuration are an order of magnitude lower than the ones computed in Reynaud et al. 2021 [4] for a transonic configuration. Indeed, as described in [4], the transonic regime is more critical in terms of unsteady loads for a space launcher. At the altitudes corresponding to a transonic regime, a lower Jet Pressure Ratio (JPR) could furthermore correspond to a flight configuration without jet collision [41] and thus with a flow topology notably different from the one studied here. Further computations using the present numerical tools to treat a transonic multi-nozzle configuration with hot propulsive jets could thus be the next step to guide the design of space launcher for this critical flight regime. The realisation of experimental studies on such a configuration would of course be necessary to assess the accuracy of the numerical studies. Such detailed databases are unfortunately currently missing in the open literature.

## 4.5 Spectral analysis



(a) Instantaneous wall pressure coefficient.



(b) Fluctuating wall pressure coefficient.

**Fig. 15:** Iso-contours of wall pressure fluctuations in the base area.

The additional information given by the analysis of the spectral content of the pressure fluctuations is useful for the mechanical design of the afterbody components and can help identify the fluid phenomena driving the flow.

#### 4.5.1 One-point analysis

The one-sided Power Spectral Density (PSD) function of pressure fluctuations, named  $G(f)$  and expressed in  $\text{Pa}^2/\text{Hz}$  describes how the rms value of pressure

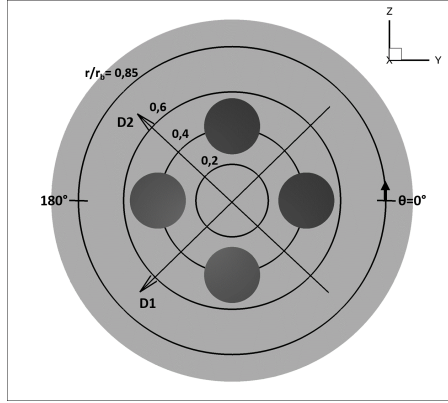


**Fig. 16:** Description of the base geometry for the study of pressure fluctuations.

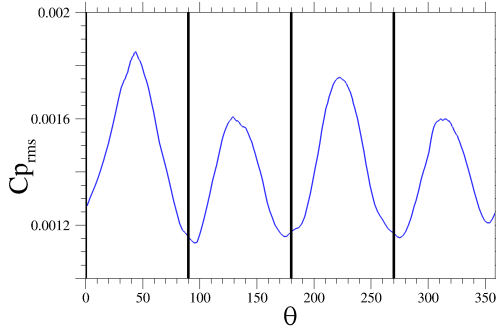


**Fig. 17:** Angular distribution of  $Cp_{rms}$  on the  $r/r_b = 0.85$  ring. Vertical bars represent 90, 180, and 270 degrees.

fluctuations  $p_{rms}$  previously described is distributed in frequency according to:

$$p_{rms}^2 = \int_0^{\infty} G(f) d(f) \quad (3)$$

These spectra are computed using the classical Welch periodogram [42] on a signal of total duration  $T = 62.5T_S$ , where  $T_S$  is the vortex shedding period (i.e. 100 ms in physical time). The PSD fluctuations are expressed as a function of the Strouhal number based on base diameter  $St_D = \frac{f \times D_b}{U_{\infty}}$ . For uni-nozzle configuration, one must remember that an important contribution to pressure fluctuations has been identified as an anti-symmetric ( $m = 1$ ) mode occurring at a Strouhal number  $St_D \approx 0.2$  [40]. In the following, we investigate if this characteristic feature for canonical flows is still showed in this complex engine bay afterbody flow.

To begin with, the spectral content of wall pressure signals is obtained by data sampling on the  $r/r_b=0.85$  ring of the launcher base (see Figure 16 for a reminder

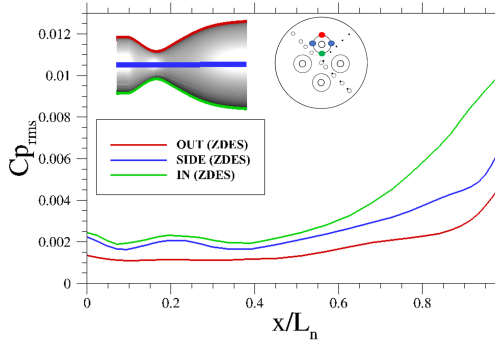


**Fig. 18:**  $Cp_{rms}$  distribution along the nozzle generating lines.

of the base geometry). We first focus on the PSD for a probe located at  $\theta = 225^\circ$ , i.e., in a plane between two nozzles (Figure 19b). This spectra displays several features namely a peak around  $St_D \approx 0.2$  (classically attributed to a vortex shedding phenomenon), a succession of peaks located in the range  $St_D \in [0.5, 2]$ , that will be discussed in the following, and a broadband contribution in the range  $St_D \in [4, 10]$  due to small-scale turbulence. The probe located at  $\theta = 180^\circ$  (Figure 19a) shows similar properties but the broadband contribution ( $St_D \in [4; 10]$ ) seems strongly attenuated. According to the results presented in [43], the broadband contribution in the range  $St_D \in [4, 10]$  can be associated with fluctuations induced by Kelvin-Helmholtz instabilities in the initial zone of the annular mixing layer.

To get further insight into the physical origin of the PSD peaks observed in the frequency range  $St_D \in [0.5, 2]$ , one can follow the analogy between the afterbody flow topology and a supersonic cavity proposed by Wong et al. 2007 [37] (see Figure 8). For such a cavity, the unsteady behaviour of the flow is driven by Rossiter modes ( $Rm$ ) observed experimentally [44, 45] and numerically [23, 46] in the literature. These modes are generated by a feedback loop linked to the convection of hydrodynamic instabilities in the mixing layer. These instabilities are generated by the separation at the upstream wall and travelled at the speed  $k_c * U_\infty$  towards the downstream wall (in the present case: the propulsive jet boundary) where their impact generates pressure waves which propagate in the upstream direction (with a dephasing factor  $r_c$ )[23] in the subsonic part of the base flow. To estimate the Strouhal number  $St_{Db|Rm}$  of these modes in the present case, an adaptation of the Rossiter [44] formula is proposed to take into account the temperature of the flow in the recirculation zone:

$$St_{Db|Rm} = \frac{D_b}{L_c} \frac{m - r_c}{U_\infty / a_c + 1/k_c} \quad (4)$$

The chosen parameters are  $k_c = 0.57$  to estimate the instabilities convection velocity and a dephasing factor  $r_c=0.25$  (both recommended for cavities with dimension between  $L_c/D_c = 1$  and 2 [44]), a mean sound velocity  $a_c \approx 760 \text{ m.s}^{-1}$  in the recirculation zone and  $L_c = X_r = 1,35 \times L_n = 0.15525 \text{ m}$  according to ZDES results (see figure 7a). The formula then provides the following values for the first

three cavity modes:  $St_{Db|R1} = 0.49$ ,  $St_{Db|R2} = 1.14$ ,  $St_{Db|R3} = 1.8$ . These frequencies obtained for a supersonic cavity with  $M_\infty = 2.75$  are coherent with the peaks observed in the range  $St_{Db} \in [0.5, 2]$ . However, these frequencies do not corresponds exactly to the peaks noticed on Figure 19b. However, one can note that the under-predicted base pressure is associated to the prediction of the temperature and thus the sound speed in the recirculation zone. As a consequence, this observation can have an impact on the use of such an expression for the characteristic modes, in analogy to the Rossiter formula. Similar analyses on less complex configurations could be realised in a future work to support this hypothesis.

The vortex shedding frequency  $St_D \approx 0.2$  therefore still plays a significant role in the dynamics of the flow as discussed in the next section.

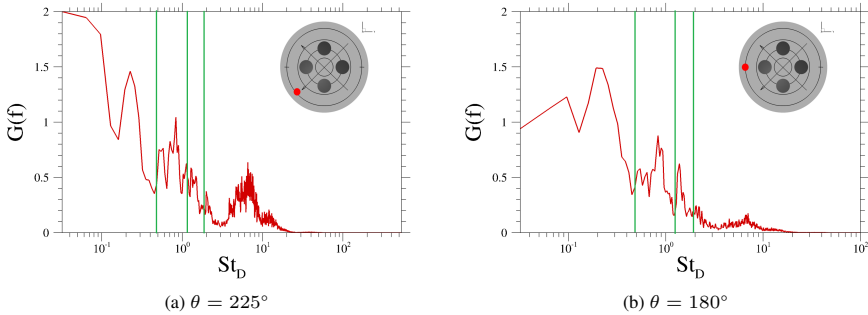


**Fig. 19:** Power spectral density  $G(f)$  [ $\text{Pa}^2 \cdot \text{Hz}^{-1}$ ] of pressure fluctuations on the base of the launcher. Green lines represent the calculated Rossiter modes.

#### 4.5.2 Two-point analysis

To get a better knowledge of the spatial organisation of the fluctuating pressure field, one can consider the azimuthal coherence between two pressure transducers [4, 24, 40]. Indeed, as the base pressure is  $2\pi$ -periodic, one can decompose the pressure field into azimuthal Fourier modes. As an example, the coherence  $C(f, \Delta\phi)$  between two probes located on the  $r/r_b=0.85$  ring and separated by an angle  $\Delta\phi$  can be decomposed in azimuthal modes as follows:

$$C_r(f, \Delta\phi) = \sum_{m=0}^{\infty} C_{r,m}(f) \cos(m\Delta\phi) \quad (5)$$

Figure 20 shows the  $C_{r,m}$  spectrum for the first three azimuthal modes for a ring of sensors located at  $r/r_b = 0.85$ . The axisymmetric mode ( $m = 0$ ) is confined at low frequencies. The contribution of the ovalization mode ( $m = 2$ ) is not significant over the whole frequency range. Of great interest is the spectrum of  $C_{r,1}$  which displays a peak near  $St_{Db} \approx 0.2$  and shows that up to 80% of the pressure fluctuations at this frequency are due to the antisymmetric mode  $m = 1$ . Let us be reminded

that the  $m = 1$  mode corresponds to an antiphase relationship between probes facing each other yielding to the so-called buffet loads [7, 40]. This important feature is also observed in more canonical flows [24, 36, 47, 48] showing the robustness of the dynamics of the antisymmetric mode in launcher base flows.

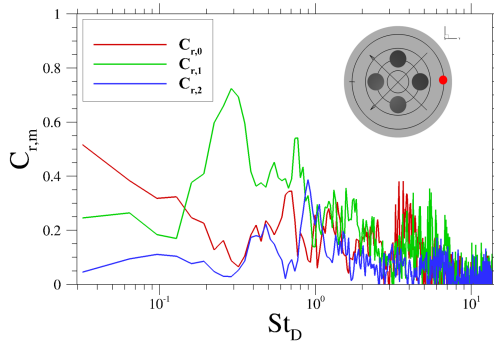


**Fig. 20:** Contribution of the first three azimuthal modes to pressure fluctuations on the  $r/r_b = 0.85$  ring (initial point at  $0^\circ$ , aligned with a nozzle).

## 5 Conclusion

The flow dynamics of a four-nozzle afterbody has been investigated numerically with a scale-resolving approach. Assuming a two-species flow, an advanced numerical simulation has been performed taking advantage of both the automatic mode of ZDES namely Mode 2 (2020) which allows the RANS/LES interface to be set dynamically and a recently developed hybrid scheme that ensures robustness when shock waves occur and low dissipation levels in vortical regions. The numerical results are compared with standard RANS calculations as well as with other results published in the open literature.

Concerning the mean pressure base, it is shown experimentally that an important characteristic is reproduced namely a constant level at the base of the afterbody. This important aspect is not recovered with a RANS approach while ZDES mode 2 (2020) simulates this salient feature. The analysis of the pressure fluctuations ( $C_{p_{rms}}$ ) revealed high level of fluctuations that can reach up to 1% of the dynamic pressure in the central region of the base (i.e. between the four nozzles). Furthermore, one-point spectral analyses reveal the occurrence of a large scale dynamics related to a Strouhal number  $St_{Db} = 0.2$  together with other peaks at higher frequencies. An analogy is discussed with the occurrence of these peaks with those observed for supersonic cavity flows as suggested by Wong et al. [37].

The dynamics of this complex engine bay flow shares similar properties with its axisymmetric counterpart. Indeed, a two-point spectral analysis reveals that up to 80% of the energy of the pressure fluctuations are due to the antisymmetric mode  $m = 1$  at a dimensionless frequency  $St_{Db} = 0.2$ .

This shows the robustness of mode  $m = 1$  which is observed for both simple and launcher base flows. Accurate validation of space launcher engine systems in extreme aerothermodynamics conditions will also require experimental databases which are still missing in the open literature.

**Acknowledgments.** The authors wish to thank the Centre National d'Études Spatiales (CNES) for financial support. The Ph.D. work of J. Reynaud is funded by CNES and ONERA. In addition, all the people involved in the evolution of the FLU3M code are warmly thanked.

## Declarations

- The thesis of Jolan Reynaud is funded by CNES and ONERA.
- The authors have no competing interests to declare that are relevant to the content of this article.
- All authors contributed to the study conception and design. Material preparation, data collection and analysis were performed by Jolan Reynaud under the supervision of Pierre-Elie Weiss and Sébastien Deck. The first draft of the manuscript was written by Jolan Reynaud, Pierre-Elie Weiss and Sébastien Deck. All authors commented on previous versions of the manuscript. All authors read and approved the final manuscript.

## References

- [1] Musial, N.T., Ward, J.J.: Base flow characteristics for several four-clustered rocket configurations at Mach numbers from 2.0 to 3.5. Technical report, NASA (1961)
- [2] Sagaut, P., Deck, S.: Large Eddy Simulation for Aerodynamics: Status and perspectives. *Philosophical Transactions of the Royal Society A: Mathematical, Physical and Engineering Sciences* **367**(1899), 2849–2860 (2009). <https://doi.org/10.1098/rsta.2008.0269>
- [3] Deck, S., Gand, F., Brunet, V., Khelil, S.B.: High-fidelity simulations of unsteady civil aircraft aerodynamics: stakes and perspectives. application of zonal detached eddy simulation. *Philosophical Transactions of the Royal Society A: Mathematical, Physical and Engineering Sciences* **372**(2022), 20130325 (2014). <https://doi.org/10.1098/rsta.2013.0325>
- [4] Reynaud, J., Weiss, P.-É., Deck, S.: Numerical workflow for scale-resolving computations of space launcher afterbody flows with and without jets. *Computers and Fluids* **226**(104994) (2021)
- [5] Statnikov, V., Stephan, S., Pausch, K., Meinke, M., Radespiel, R., Schröder, W.: Experimental and numerical investigations of the turbulent wake flow of a generic space launcher at  $M_\infty = 3$  and  $M_\infty = 6$ . *CEAS Space Journal* **8**(2), 101–116 (2016)

- [6] Pain, R., Weiss, P.-É., Deck, S.: Zonal Detached Eddy Simulation of the Flow Around a Simplified Launcher Afterbody. *AIAA Journal* **52**(9), 1967–1979 (2014). <https://doi.org/10.2514/1.j052743>
- [7] Weiss, P.-É., Deck, S.: On the coupling of a zonal body-fitted/immersed boundary method with ZDES: Application to the interactions on a realistic space launcher afterbody flow. *Computers & Fluids* **176**, 338–352 (2018). <https://doi.org/10.1016/j.compfluid.2017.06.015>
- [8] Gusman, M., Housman, J., Kiris, C.: Best practices for cfd simulations of launch vehicle ascent with plumes-overflow perspective. In: 49th AIAA Aerospace Sciences Meeting Including the New Horizons Forum and Aerospace Exposition, p. 1054 (2011)
- [9] Mehta, M., Canabal, F., Tashakkor, S.B., Smith, S.D.: Base heating sensitivity study for a 4-cluster rocket motor configuration in supersonic freestream. *Journal of Spacecraft and Rockets* Vol. 50, No. 3, May/June 2013 (2013)
- [10] Pu, P., Jiang, Y.: Assessing turbulence models on the simulation of launch vehicle base heating. *International Journal of Aerospace Engineering* **2019**, 1–14 (2019). <https://doi.org/10.1155/2019/4240980>
- [11] Deck, S., Renard, N.: Towards an enhanced protection of attached boundary layers in hybrid RANS/LES methods. *Journal of Computational Physics* **400**, 108970 (2020). <https://doi.org/10.1016/j.jcp.2019.108970>
- [12] Reynaud, J., Weiss, P.-É., Deck, S., Guillen, P.: A comprehensive framework for high fidelity computations of two-species compressible turbulent flows. *Journal of Computational Physics* **462**, 111222 (2022). <https://doi.org/10.1016/j.jcp.2022.111222>
- [13] Huff, V.N., Fortini, A., Gordon, S.: Theoretical performance of jp-4 fuel and liquid oxygen as a rocket propellant ii: equilibrium composition. Technical report, NACA (1956)
- [14] Baurle, R.A., Edwards, J.R.: Hybrid Reynolds-Averaged/Large-Eddy Simulations of a coaxial supersonic freejet experiment. *AIAA Journal* **48**(3), 551–571 (2010). <https://doi.org/10.2514/1.43771>
- [15] Clifton, C.W., Cutler, A.D.: A supersonic argon/air coaxial jet experiment for computational fluid dynamics code validation (2007)
- [16] Reynaud, J., Weiss, P.-É., Deck, S.: Towards Binary Gas Mixture ZDES for Space Launcher Base Flow Prediction. In: 55 Th 3AF International Conference on Applied Aerodynamics Poitiers - France (2020+1)
- [17] Mary, I., Sagaut, P.: Large Eddy Simulation of Flow Around an Airfoil Near



- 24 *On the use of bi-species ZDES for multi-nozzle space launcher configurations*  
Stall. AIAA Journal **40**(6), 1139–1145 (2002). <https://doi.org/10.2514/2.1763>
- [18] Pamiès, M., Weiss, P.-É., Garnier, E., Deck, S., Sagaut, P.: Generation of synthetic turbulent inflow data for large eddy simulation of spatially evolving wall-bounded flows. *Physics of Fluids* **21**(4), 045103 (2009). <https://doi.org/10.1063/1.3103881>
- [19] Gand, F., Deck, S., Brunet, V., Sagaut, P.: Flow dynamics past a simplified wing body junction. *Physics of Fluids* **22**(11), 115111 (2010). <https://doi.org/10.1063/1.3500697>
- [20] Deck, S., Renard, N., Laraufie, R., Weiss, P.-É.: Large-scale contribution to mean wall shear stress in high-Reynolds-number flat-plate boundary layers up to 13650. *Journal of Fluid Mechanics* **743**, 202–248 (2014). <https://doi.org/10.1017/jfm.2013.629>
- [21] Deck, S., Weiss, P.-É., Renard, N.: A rapid and low noise switch from rans to wmls on curvilinear grids with compressible flow solvers. *Journal of Computational Physics* **363**, 231–255 (2018)
- [22] Simon, F., Deck, S., Guillen, P., Sagaut, P., Merlen, A.: Numerical simulation of the compressible mixing layer past an axisymmetric trailing edge. *Journal of Fluid Mechanics* **591**, 215–253 (2007)
- [23] Larchevêque, L., Sagaut, P., Lê, T.-H., Comte, P.: Large-eddy simulation of a compressible flow in a three-dimensional open cavity at high Reynolds number. *Journal of Fluid Mechanics* **516**, 265 (2004)
- [24] Weiss, P.-É., Deck, S., Robinet, J.-C., Sagaut, P.: On the dynamics of axisymmetric turbulent separating/reattaching flows. *Physics of Fluids* **21**(7), 075103 (2009). <https://doi.org/10.1063/1.3177352>
- [25] Weiss, P.-É., Deck, S.: Numerical investigation of the robustness of an axisymmetric separating/reattaching flow to an external perturbation using zdes. *Flow, turbulence and combustion* **91**(3), 697–715 (2013)
- [26] Ducros, F., Ferrand, V., Nicoud, F., Weber, C., Darracq, D., Gacherieu, C., Poinso, T.: Large-eddy simulation of the shock/turbulence interaction. *Journal of Computational Physics* **152**(2), 517–549 (1999). <https://doi.org/10.1006/jcph.1999.6238>
- [27] Liou, M.-S.: A sequel to AUSM: AUSM+. *Journal of Computational Physics* **129**(2), 364–382 (1996). <https://doi.org/10.1006/jcph.1996.0256>
- [28] Pechier, M., Guillen, P., Cayzac, R.: Magnus effect over finned projectiles. *Journal of Spacecraft and Rockets* **38**(4), 542–549 (2001)

- [29] Deck, S., Duveau, P., d’Espiney, P., Guillen, P.: Development and application of spalart–allmaras one equation turbulence model to three-dimensional supersonic complex configurations. *Aerospace Science and Technology* **6**(3), 171–183 (2002)
- [30] Deck, S.: Zonal-Detached-Eddy Simulation of the flow around a high-lift configuration. *AIAA Journal* **43**(11), 2372–2384 (2005). <https://doi.org/10.2514/1.16810>
- [31] Deck, S.: Recent improvements in the Zonal Detached Eddy Simulation (ZDES) formulation. *Theoretical and Computational Fluid Dynamics* **26**(6), 523–550 (2011). <https://doi.org/10.1007/s00162-011-0240-z>
- [32] Deck, S., Renard, N., Laraufie, R., Sagaut, P.: Zonal Detached Eddy Simulation (ZDES) of a spatially developing flat plate turbulent boundary layer over the reynolds number range  $3\,150 \leq Re_\theta \leq 14\,000$ . *Physics of Fluids* **26**(2), 025116 (2014)
- [33] Vaquero, J., Renard, N., Deck, S.: Outer layer turbulence dynamics in a high-reynolds-number boundary layer up to  $re_\theta \approx 24,000$  recovering from mild separation. *Journal of Fluid Mechanics* **942**, 42 (2022)
- [34] Deck, S., Laraufie, R.: Numerical investigation of the flow dynamics past a three-element aerofoil. *Journal of Fluid Mechanics* **732**, 401–444 (2013). <https://doi.org/10.1017/jfm.2013.363>
- [35] Spalart, P.R., Allmaras, S.R.: A one-equation turbulence model for aerodynamic flows. *La Recherche Aéronautique* (1), 5–21 (1994)
- [36] Pain, R., Weiss, P.-É., Deck, S., Robinet, J.-C.: Large scale dynamics of a high Reynolds number axisymmetric separating/reattaching flow. *Physics of Fluids* **31**(12), 125119 (2019). <https://doi.org/10.1063/1.5121587>
- [37] Wong, H., Meijer, J., Schwane, R.: Experimental and theoretical investigation of base-flow buffeting on ariane5 launch vehicles. *Journal of propulsion and power* **23**(1), 116–122 (2007)
- [38] Simon, F., S., Guillen, P., Cayzac, R., Merlen, A.: Zonal-Detached-Eddy Simulation of Projectiles in the subsonic and transonic regimes. *AIAA Journal* **45**(7), 1606–1619 (2007). <https://doi.org/10.2514/1.26827>
- [39] Kawai, S., Fujii, K.: Time-series and time-averaged characteristics of subsonic to supersonic base flows. *AIAA Journal* **45**(1), 289–301 (2007). <https://doi.org/10.2514/1.24601>
- [40] Deck, S., Thorigny, P.: Unsteadiness of an axisymmetric separating-reattaching flow: Numerical investigation. *Physics of Fluids* **19**(6), 065103 (2007). <https://doi.org/10.1063/1.2748103>

[//doi.org/10.1063/1.2734996](https://doi.org/10.1063/1.2734996)

- [41] Faheem, M., Khan, A., Kumar, R., Khan, S.A., Asrar, W., Sapardi, A.M.: Experimental study on the mean flow characteristics of a supersonic multiple jet configuration. *Aerospace Science and Technology* **108**, 106377 (2021). <https://doi.org/10.1016/j.ast.2020.106377>
- [42] Welch, P.: The use of fast fourier transform for the estimation of power spectra: A method based on time averaging over short, modified periodograms. *IEEE Transactions on Audio and Electroacoustics* **15**(2), 70–73 (1967). <https://doi.org/10.1109/tau.1967.1161901>
- [43] Weiss, P.-E.: Simulation numérique et analyse physique d'un écoulement d'arrière-corps axisymétrique et application au contrôle des charges latérales. PhD thesis, Paris 6 (2010)
- [44] Rossiter, J.: Wind tunnel experiments on the flow over rectangular cavities at subsonic and transonic speeds. RAE Technical Report No. 64037 (1964)
- [45] Zhuang, N., Alvi, F.S., Alkislal, M.B., Shih, C.: Supersonic cavity flows and their control. *AIAA Journal* **44**(9), 2118–2128 (2006). <https://doi.org/10.2514/1.14879>
- [46] Larchevêque, L., Sagaut, P., Mary, I., Labbé, O., Comte, P.: Large-eddy simulation of a compressible flow past a deep cavity. *Physics of Fluids* **15**(1), 193–210 (2003). <https://doi.org/10.1063/1.1522379>
- [47] Marié, S., Deck, S., Weiss, P.E.: From pressure fluctuations to dynamic loads on axisymmetric step flows with minimal number of kulites. *Computers & Fluids* **39**(5), 747–755 (2010). <https://doi.org/10.1016/j.compfluid.2009.12.001>
- [48] Weiss, P.-É., Deck, S.: Control of the antisymmetric mode ( $m = 1$ ) for high Reynolds axisymmetric turbulent separating/reattaching flows. *Physics of Fluids* **23**(9), 095102 (2011). <https://doi.org/10.1063/1.3614481>